Scilight

Hydrology and Water Resources
https://www.sciltp.com/journals/hwr

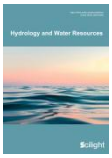

Article

Groundwater Storage as a Key Driver of Subannual Streamflow Variability

Yongqiang Zhang [1,*], Hongxing Zheng [2], Changming Liu [1], L. Ruby Leung [3], Chunmiao Zheng [4], Dongdong Kong [5] and Günter Blöschl [6]

[1] Key Laboratory of Water Cycle and Related Land Surface Processes, Institute of Geographic Sciences and Natural Resources Research, Chinese Academy of Sciences, Beijing 100101, China
[2] CSIRO Environment, Black Mountain, Canberra, ACT 2601, Australia
[3] Pacific Northwest National Laboratory, Richland, WA 99352, USA
[4] School of the Environment and Sustainable Engineering, Eastern Institute of Technology, Ningbo 315000, China
[5] Department of Atmospheric Science, School of Environmental Studies, China University of Geosciences, Wuhan 430074, China
[6] Institute of Hydraulic and Water Resources Engineering, Technische Universität Wien, Vienna 1040, Austria
* Correspondence: zhangyq@igsnrr.ac.cn

How To Cite: Zhang, Y.; Zheng, H.; Liu, C.; et al. Substantial Role of Groundwater Storage to Subannual Streamflow Variability. *Hydrology and Water Resources* **2025**, *1*(1), 2. https://doi.org/10.53941/hwr.2026.100002.

Received: 4 August 2025
Revised: 30 August 2025
Accepted: 2 September 2025
Published: 16 September 2025

Abstract: Precipitation is the largest flux of the global land hydrological cycle and is widely regarded as the dominant contributor to catchment streamflow. For decades, it has been the primary basis for attributing streamflow variability at annual to decadal timescales. Yet, the relative importance of other hydrological processes in controlling streamflow across different timescales remains unclear. As a measure of the sensitivity of streamflow to changes in its driving variables, streamflow elasticity has been used to quantify streamflow sensitivity to environmental changes. Here, using data from 1628 catchments distributed across the globe, we show that the elasticity of streamflow to precipitation at monthly and seasonal scales is far smaller than the annual elasticity because groundwater storage substantially buffers streamflow variability at subannual timescales, especially in water-limited regions. Therefore, groundwater storage must be considered alongside precipitation and potential evaporation to provide a comprehensive understanding of streamflow responses to climate variability and change. Our results underscore the important need for improving modeling of groundwater storage variability for robust projections of hydrological impacts under a changing climate.

Keywords: streamflow; groundwater; storage; subannual variability; catchment

1. Introduction

Water crisis is one of the most consequential global risks, and is closely related to climate change and social-economic growth [1–7] over the next several decades. For sustainable development in regions under water stress [8], it is crucial to identify the major drivers contributing to water availability change and understand the catchment resilience for characterizing the response of riverine ecosystems to external disturbances and the related socioeconomic impact [1,6,9–13].

The resilience of catchment streamflow to climate variability and change can be assessed using the concept of streamflow elasticity, which quantifies the sensitivity of streamflow to climate drivers such as precipitation and potential evaporation. With smaller elasticity, streamflow sensitivity to climate is lower, indicating a stronger ability of the catchment to buffer external changes and hence, stronger catchment resilience [14,15].

Among all the hydroclimate drivers controlling streamflow variability, precipitation is widely considered the dominant factor because of its large contribution to streamflow. This notion was reinforced by previous studies attributing streamflow variation at annual to decadal timescale with little consideration of the effect of groundwater

storage [16–18]. Annual streamflow elasticity has been used to quantify the impacts of climate on streamflow for several decades [11,13,17–19]. During precipitation events, portions of the precipitation are stored in the pores and fractures of the subsurface media as groundwater storage, which gradually contributes baseflow to the total catchment streamflow. These hydrological processes suggest that groundwater storage buffers streamflow response to high frequency climate variability, enhancing streamflow resilience to climate change (Supporting Information, Figure S1). Although the buffering effect of groundwater storage on hydrologic response is already known [20–26], the relative contributions of groundwater storage and climate factors to streamflow variability remain unknown across monthly, seasonal, and annual timescales.

Considering the impacts of both climate and groundwater storage, we investigate streamflow variability within a data-driven framework by attributing three dominant drivers (two climate drivers of precipitation and potential evaporation, and groundwater storage) of streamflow variability at different timescales. This framework is built on the concept of elasticity of streamflow [17,18]. We use 1628 small catchments widely distributed across the globe, each having more than 20 years of daily observations, and a combination of 15 approaches to estimate groundwater storage and potential evaporation. This results in probabilistic estimates of elasticities of streamflow with respect to the two climate drivers and groundwater storage, accounting for uncertainties in the approach and variations across catchments (see Methods). Using the estimated elasticities, we appraise the relative contributions of precipitation, potential evaporation, and groundwater storage to streamflow variability.

2. Data

2.1. Meteorological and Albedo Data

Daily precipitation, air temperature, vapor pressure, shortwave downward radiation, longwave downward radiation and wind speed were obtained from the 0.25-degree resolution Princeton Global Forcing (PGF) dataset for the period of 1948 to 2015 [27,28].

Three potential evaporation datasets were derived from the Priestley-Taylor [29], Penman [30] and Morton's method for wet environment areal evaporation [31] by using air temperature, vapor pressure, shortwave downward radiation, longwave downward radiation, wind speed, obtained from the PGF dataset. We used albedo obtained from the MODIS MOD43C1 product (https://www.umb.edu/spectralmass/terra_aqua_modis/modis_user_guide_v004/mod43c1_cmg_albedo_product, accessed on 5 December 2021) to calculate the net shortwave radiation. The original 500m resolution albedo was resampled to 0.25-degree resolution using the nearest-neighbour sampling approach to match the PGF dataset. We used monthly mean albedo obtained from 2000 to 2006 for each catchment. The albedo for each grid cell was area-weight averaged for catchment albedo.

2.2. Streamflow Data

The streamflow data used in this study were collated from two studies [32,33] that obtained data from four sources: Global Runoff Data Centre (GRDC, located in Germany, http://www.bafg.de/GRDC/EN/Home/homepage_node.html, accessed on 20 August 2018); the Geospatial Attributes of Gages for Evaluating Streamflow (GAGES)-II database [34], the Australian Bureau of Meteorology (http://www.bom.gov.au/water/hrs/, accessed on 30 September 2017), and the Chinese Academy of Sciences. To solidly attribute streamflow variation, we setup the following selection criteria for selecting high quality streamflow data: (1) unregulated without major dam regulations, diversions and local withdrawals; (2) small with catchment area less than <10,000 km^2 to minimize the impact of streamflow routing process on baseflow separation [35]; and (3) more than 20 years of daily observations in the period of 1948 to 2015. At the end, this study selected 1628 unregulated small catchments for our analysis, for which there are 591, 885 and 152 catchments located in dry regions, equitant regions and wet regions, respectively. Classification of the catchments is detailed in Section 3.1.

To exclude regulated catchments, major dam locations were obtained from four sources: (i) the Global Reservoir and Dam (GRanD) database (v1.1) [36]; (ii) International Commission of Large Dams; (iii) Meridian World Data (http://www.meridianworlddata.com/, accessed on 20 May 2019) and (iv) National Land and Water Resources Audit of Australia (http://www.nlwra.gov.au/, accessed on 1 July 2022).

3. Methods

3.1. Overall Framework

We start a conceptual framework for hydrological processes for a particular catchment. Fundamentally, catchment water source comes from atmospheric precipitation (P). When P reaches the catchment, it is partitioned into three parts: evaporation, surface runoff and soil water. Evapotranspiration is water evaporated to atmosphere from land surface by soil evaporation, vegetation transpiration, and evaporation from intercepted water by the canopy. Surface runoff is the flow over land surface contributing to river flow. Soil water is the water infiltrating into soil. Part of the soil water is returned to the atmosphere through soil evaporation and transpiration; the rest is partitioned into two parts: inter-flow contributing to streamflow (Q) and recharge into groundwater storage. The discharge from groundwater into the stream is called baseflow.

The conceptualized hydrograph in Figure 1 shows that the total streamflow comprises of three components: surface runoff, inter-flow and baseflow. The baseflow can be separated from the hydrograph by the numerical approaches. A linear reservoir model [36,37] is generally considered as a good approximation of the relationship between baseflow and groundwater storage [38–40]. Hence, once the variability in baseflow is known, the groundwater storage variability can be estimated reversely.

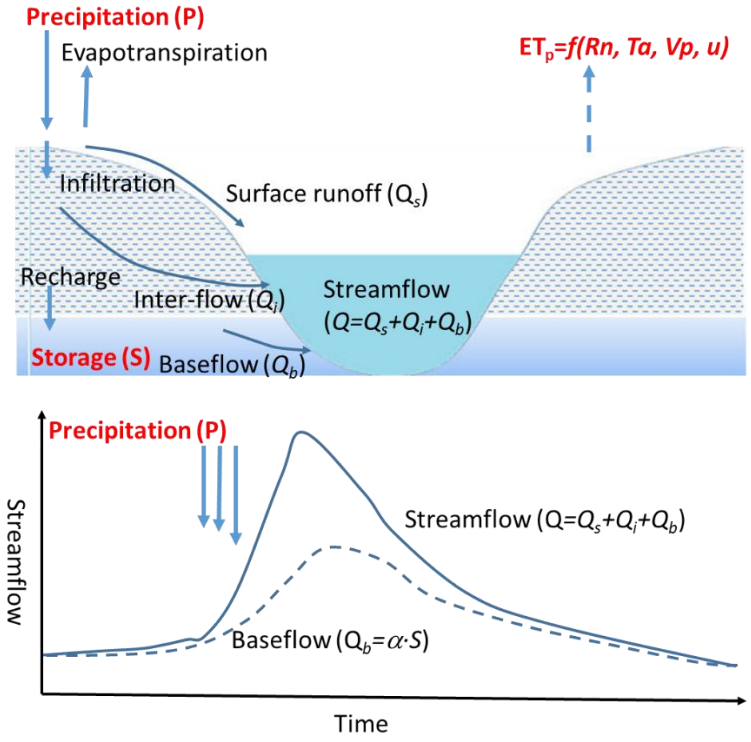

Figure 1. Conceptual diagram of hydrological processes at the catchment scale and the estimate of storage on the basis of observed streamflow record. In the diagram, *PET* is the potential evaporation, which is a function of net radiation (R_n), air temperature (T_a), vapor pressure (V_p) and wind speed (u); α is the recession constant.

For better understanding the role of groundwater storage in moderating streamflow availability, we partition the catchments into different climate regimes defined by the aridity index (mean annual potential evaporation divided by mean annual precipitation, AI). The higher AI is drier the catchment. Based on the recommendation from McVicar et al. (2012) [31], we grouped the catchments into three categories: water-limited regions (dry regions with aridity index >1.35), equitant regions with aridity index of 0.76–1.35, and energy-limited regions (wet/cold regions with aridity index <0.76).

3.2. Modelling Framework for Attributing Streamflow Variation

To assess the effect of temporal scale on variation of Q, for a given catchment, the variation of streamflow is investigated at monthly (January to December), seasonal (three-month aggregated) and annual (sum of the 12 months) scales. At the annual scale, the variation of Q is the difference between the streamflow of a given calendar year and that of the long-term mean:

$$\Delta Q_i = Q_i - \overline{Q}, \tag{1}$$

where Q_i is the annual streamflow at the i^{th} year, ΔQ_i is the annual streamflow variability at the i^{th} year, and $\overline{Q}$ is the mean annual streamflow. At monthly or seasonal scale, the variation of Q is:

$$\Delta Q_{i,j} = Q_{i,j} - \bar{Q}_j \quad \text{with} \quad Q_i = \sum_{j=1}^{n} Q_{i,j} \; and \; \Delta Q_i = \sum_{j=1}^{n} \Delta Q_{i,j}, \tag{2}$$

where $Q_{i,j}$ is the monthly (or seasonal) streamflow at the j^{th} month (or season) and i^{th} year, $\Delta Q_{i,j}$ is the monthly (or seasonal) streamflow variability at the j^{th} month (or season) and i^{th} year, $\bar{Q}_j$ is the mean monthly or seasonal streamflow at the j^{th} month (or season), n is the number of months (=12) or number of seasons (=4). The variation of the forcing variables is defined the same way as that of streamflow.

For all three temporal scales, the forcing variables considered include P, potential evaporation (PET) and catchment groundwater storage (S). The Q, P and PET are the flux variables and aggregated from the entire temporal scale. In comparison, S is the state variable and therefore is obtained from its magnitude at the start date of each month (for monthly scale), start date of each season (for seasonal scale) or start date of each year (for annual scale). The variation of streamflow is decomposed as a function of P, PET and S:

$$\frac{\Delta Q}{\overline{Q}} = \varepsilon_P \frac{\Delta P}{\overline{P}} + \varepsilon_{PET} \frac{\Delta PET}{\overline{PET}} + \varepsilon_S \frac{\Delta S}{\overline{S}} + \epsilon, \tag{3a}$$

or

$$\frac{\Delta Q_j}{\bar{P}_j} = \varepsilon_{P,j} \frac{\Delta P_j}{\bar{P}_j} + \varepsilon_{PET_j} \frac{\Delta PET_j}{\bar{P}_j} + \varepsilon_{S,j} \frac{\Delta S_j}{\overline{S}_j} + \epsilon_j, \tag{3b}$$

where $\overline{P}$ is the mean annual precipitation, $\overline{PET}$ is the mean annual potential evaporation, $\bar{P}_j$ the mean monthly (or seasonal) precipitation at the j^{th} month (or season), $\overline{PET}_j$ is the mean monthly (or seasonal) potential evaporation at the j^{th} month (or season), ϵ denotes systematic errors, which are assumed to be relatively smaller and are taken as residues.

Considering only the three driving variables, we can define the Relative Contribution (RC):

$$RC_P + RC_{PET} + RC_S = 1 \text{ or } RC_{P,j} + RC_{PET_j} + RC_{S,j} = 1, \tag{4a}$$

where,

$$RC_X = \frac{C_X}{C_P + C_{PET} + C_S} \text{ or } RC_{X,j} = \frac{C_{X,j}}{C_{P,j} + C_{PET_j} + C_{S,j}}, \tag{4b}$$

where C_P, C_{PET}, and C_S are the contribution of P, PET, and S respectively.

3.3. Estimating Potential Evaporation and Catchment Storage

Three models were used to calculate the potential evaporation for the catchments, which include the Priestley-Taylor [29], Penman [30] and Morton's method for wet environment areal evaporation [31]. The expressions of the three models are shown at Equations (5a)–(5c), respectively.

$$PET = \lambda \frac{\Delta}{\Delta + \gamma} (R_n - G) + 6.43\lambda \frac{\Delta}{\Delta + \gamma} (1 + 0.537u_2)(e_s - e_a), \tag{5a}$$

$$1.26\lambda \frac{\Delta}{\Delta + \gamma} (R_n - G), \tag{5b}$$

$$PET = \lambda \left(14 + 1.2 \frac{\Delta}{\Delta + \gamma} R_n\right), \tag{5c}$$

where, PET is the potential evaporation (mm/d), R_n is the net radiation (MJ/m^2/d), G is soil heat flux (MJ/m^2/d), Δ is the slope of the saturation vapor pressure curve (kPa/°C), γ is the Psychrometric constant (kPa/°C), u_2 is wind speed at 2 m (m/s), e_s and e_a are saturated and actual vapor pressure (kPa), λ is the vaporization latent heat of water (=2.45 MJ/kg).

Estimation of the groundwater storage uses the assumption that the discharge (baseflow, Q_b) from the aquifer is linearly proportional to its storage [38–40], which is expressed as:

$$Q_b = \alpha S, \tag{6}$$

This linear reservoir assumption leads to the model of an exponential baseflow recession (with recession constant of α) during periods without recharging to groundwater, which is tested to be rational for a large number

of catchments according to the observed streamflow records. To estimate the storage of the catchment, we first estimate the groundwater discharge by separating the baseflow from the available daily streamflow data, and then use the estimated baseflow to derive the corresponding groundwater storage according to Equation (6).

We used five baseflow separation approaches, including four recursive digital filter approaches and one standard Institute of Hydrology algorithm [41]. The four recursive digital filter approaches are proposed by Lyne and Hollick [42], Boughton [43], Chapman and Maxwell [38] and Eckhardt [44], which are expressed respectively in Equations (7a)–(7d):

$$Q_b(t) = \alpha \cdot Q_b(t-1) + \frac{1-\alpha}{2}[Q(t) + Q(t-1)], \tag{7a}$$

$$Q_b(t) = \frac{\alpha}{1+C} \cdot Q(t-1) + \frac{C}{1+C} Q(t), \tag{7b}$$

$$Q_b(t) = \frac{\alpha}{2-\alpha} \cdot Q_b(t-1) + \frac{1-\alpha}{2-\alpha} Q(t), \tag{7c}$$

$$Q_b(t) = \frac{(1-BFI_{max}) \cdot \alpha \cdot Q_b(t-1) + (1-\alpha) \cdot BFI_{max} \cdot Q(t)}{1-\alpha \cdot BFI_{max}}. \tag{7d}$$

where $Q(t)$ is the streamflow at time t (here t is for a particular date), $Q_b(t)$ is the baseflow at time t, α is the recession constant, C is a constant and set to be 0.15; *BFImax* is a parameter representing the maximum ratio of baseflow to total runoff. As suggested by [44], we set *BFImax* = 0.80 for perennial streams with porous aquifers, *BFImax* = 0.50 for ephemeral streams with porous aquifers, and *BFImax* = 0.25 for perennial streams with hard rock aquifers. The recession constant in this study is estimated by using the master depletion curve derived using the matching strip method [45] in the HydroFlow software (version 1.0).

As mentioned above, this study used three approaches to estimate *PET* [29–31] and five approaches (Boughton-Chapman method, Chapman-Maxwell, Eckhard, Lyne and Hollick, and Standard BFI) to separate baseflow from observed streamflow, which is further used to estimate catchment storage variation. Therefore, we obtained different combinations of *PET* and *S* using 15 approaches.

3.4. Quantifying Precipitation Variability Change Impact on Streamflow Variability Change

To investigate streamflow variability change caused by a change in precipitation variability (ΔP), we evaluate 22 scenarios for ΔP increasing by 1% to 100% of $\overline{P}$ (i.e., $\Delta P/\overline{P}$ increased by 1%, 2.5%, 5%, 10%, 15%, ⋯, 100%). For each scenario, ΔP is randomly partitioned to each month. Using precipitation alone, the change in annual streamflow variability (ΔQ_c) can be estimated annually (Equation (8a) and cumulatively (Equation (8b)):

$$\Delta Q_c = \varepsilon_P \Delta\left(\frac{\Delta P}{\overline{P}}\right)\overline{Q}, \tag{8a}$$

or

$$\Delta Q_c = \sum \varepsilon_{P,j} \Delta\left(\frac{\Delta P_j}{\bar{P}_j}\right)\bar{Q}_j, \tag{8b}$$

where ε_P refers to the elasticity of streamflow Q with respect to precipitation, $\Delta(\Delta P/\overline{P})$ is the annual precipitation change scenario, $\Delta\left(\frac{\Delta P_j}{\bar{P}_j}\right)$ is the j^{th} monthly (or j^{th} season) precipitation change scenario.

The consistency of results obtained from Equations (8a) and (8b) can be evaluated using:

$$Ratio = \frac{\sum \varepsilon_{P,j} \Delta\left(\frac{\Delta P_j}{\bar{P}_j}\right)\bar{Q}_j}{\varepsilon_P \Delta\left(\frac{\Delta P}{\overline{P}}\right)\overline{Q}}, \tag{9}$$

If the *Ratio* approaches one, the mean of $\varepsilon_{P,j}$ is similar to ε_P, and therefore the change of the monthly cumulative streamflow variability is similar to the change of annual streamflow variability. For the *Ratio* far less than 1, $\varepsilon_{P,j}$ is largely less than ε_P, and therefore the change of monthly (seasonal) cumulative streamflow variability is far less than the change of annual streamflow variability.

3.5. Comparison with Global Hydrological Modelling

To use the data-driven framework fairly evaluating global hydrological modelling results, monthly simulated groundwater recharge and monthly forcing data of precipitation and potential evaporation data were obtained from each of four widely used global hydrological models (HBV-SIMREG [46], LISFLOOD [47], PCR-GLOBWB [48], and SURFEX-trip [49] through a Water Cycle Integrator portal (WCI, wci.earth2observe.eu) [28]. The global dataset covers the period of 1979–2012 at the spatial resolution of 0.5 degree. The gridded data were aggregated to each catchment using area-weighted average (i.e., ratio of grid cell within catchment multiplied by grid cell area).

3.6. Probability Diagram

We employed ternary diagrams to characterize the relative contributions of *P*, *PET*, and *S*. The ternary space ensures that the three components sum to unity, thus each point represents a unique hydroclimatic state. The plots were generated using the *R* package ggtern [50]. Probability contour lines are shown at the 10%, 30%, 50%, 70%, and 90% levels, denoting cumulative highest density regions, which are implemented by the stat_prob_2d function in the *R* package gg.layers (see Figures in Section 4). For example, the 10% contour encloses the most densely populated region, indicating that the highest-density 10% of points fall within this area, while broader contours progressively include larger proportions of the data with lower density. The red bold lines are drawn from the 50% position of each coordinate axis as perpendiculars to the opposite side, thereby partitioning the triangle into three regions. Each region corresponds to a distinct dominant control factor: the lower-left area is dominated by *S*, the lower-right area by *P*, and the upper area by PET.

4. Results

4.1. Streamflow Elasticities

For all three temporal (monthly, seasonal and annual) scales, the three drivers together explain >68% and >53% of the streamflow variability for 50% and 75% of the catchments, respectively (Supporting Information, Figure S1). Furthermore, the annual streamflow variability estimated at the three temporal scales for the three drivers corresponds well with the observations (Supporting Information, Figure S2). This indicates that the three drivers can largely explain the variability of streamflow at multiple temporal scales and perform similarly and provide us with confidence for the following analysis.

The elasticities of streamflow to precipitation and groundwater storage vary at different temporal scales. The ε_P increases from monthly to annual scales (Figure 2a). In contrast, storage elasticity decreases from monthly to annual scales (Figure 2b). Potential evaporation elasticity of streamflow shows little temporal dependence with marginal differences between the monthly, seasonal, and annual timescales (Figures S3–S5). These results indicate that monthly (or seasonal) streamflow is more resilient to precipitation changes than annual streamflow.

With the higher resilience at monthly scale, the ratio of the streamflow variability change estimated using monthly ε_P to that estimated using annual ε_P (see Equations (8) and (9)) varies from 0.2 to 0.7 (Figure 2c). This suggests that policy makers will substantially overestimate monthly streamflow changes if they simply use annual ε_P to predict monthly streamflow variability caused by climate change. These findings shown in Figure 2 suggest that groundwater storage reduces the sensitivity of streamflow to precipitation change and hence enhances catchment resilience to climate change. This buffering effect of storage [51,52] is more noticeable at shorter scales (i.e., monthly and seasonal) and becomes negligible at annual scale.

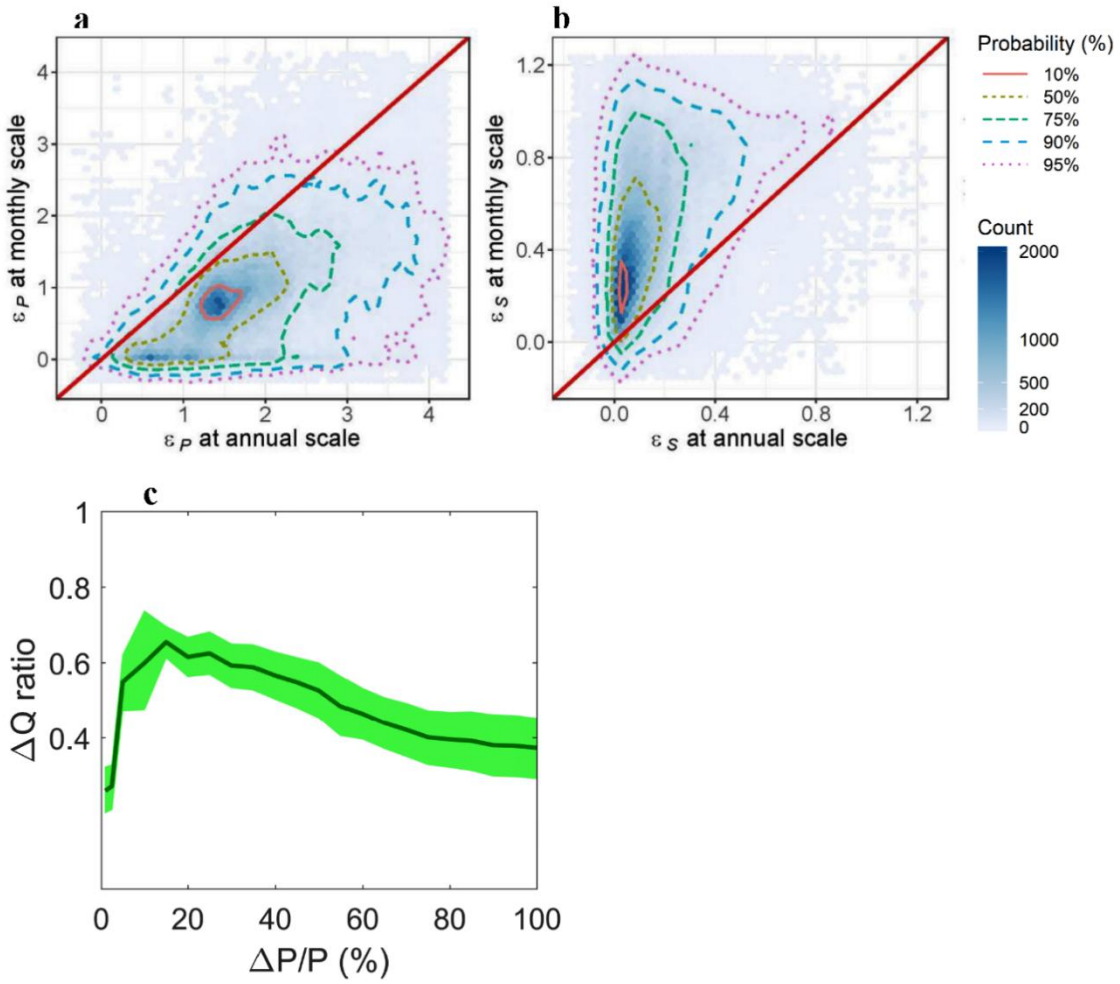

Figure 2. Temporally dependent precipitation elasticity of streamflow. (**a**) Comparison of precipitation elasticity of streamflow (ε_P) between monthly and annual scales. (**b**) Comparison of groundwater storage elasticity of streamflow (ε_S) between monthly and annual scales. (**c**) The ratio of cumulative monthly streamflow variability (Equations (8) and (9)) estimated using monthly ε_P to annual streamflow variability estimated using annual ε_P under different precipitation changes (annual precipitation variability (ΔP) divided by the mean annual precipitation ($\overline{P}$)). The space enclosed by each contour in Figure 2a,b corresponds to the probability of the elasticity values considering uncertainties in the methods and variations across catchments. The range between the 10th and 90th percentiles is shown in green and the median in dark blue. Data are from 1628 catchments using 15 approaches (three potential evaporation approaches multiplying five groundwater storage approaches).

4.2. Attributing Streamflow Variability

The relative contributions of precipitation, catchment storage and potential evaporation to streamflow variability are quantified for all 1628 catchments, which further demonstrate the substantial discrepancy between the temporal scales and the role of groundwater storage (Figure 3). At annual scale, precipitation is the dominant contributor of streamflow variability, with relative contribution (RC) of more than 50% for 77.2% of catchments (Figure 3c). In comparison, the impacts of the other two factors are smaller, both with RC > 50% for only less than 2.5% of catchments (Figure 3b,c). On a monthly scale, the contribution of groundwater storage is prominent for a large fraction of catchments, with RC > 50% for 30.9% of catchments. The contribution of precipitation is correspondingly smaller than that at the annual scale (with RC > 50% for 47.6% of catchments). The impacts of potential evaporation are small for most catchments. The relative contributions of precipitation at seasonal scale are in between those at monthly and annual scales (Supporting Information, Figures S3–S6). In general, at a longer temporal scale, the importance of precipitation in controlling streamflow variability increases while the effect of catchment storage in controlling streamflow variability fades.

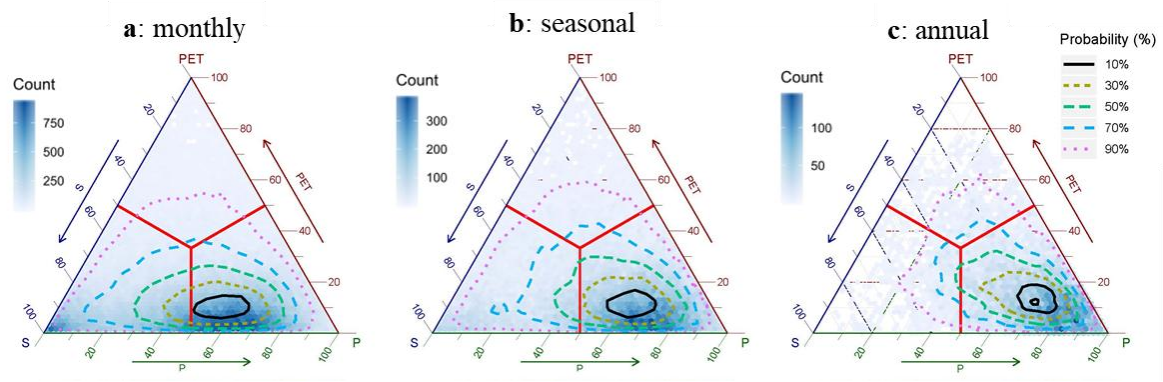

Figure 3. Relative contributions (%) of precipitation (P), groundwater storage (S) and potential evaporation (PET) to streamflow variability at monthly (**a**), seasonal (**b**), and annual (**c**) scales. The space enclosed by the contours corresponds to 10%, 30%, 50%, 70% and 90% probability, with the number of points (count) indicated using a filled color in each hexagon bin. Data are from 1628 catchments using 15 approaches.

For different climate regimes, the contribution of groundwater storage is stronger in water-limited regions (dry regions with aridity index > 1.35) than in energy-limited regions (wet/cold regions with aridity index < 0.76) (Figure 4). In comparison, the contribution of precipitation is stronger in energy-limited regions than in water-limited regions. The contrasting effect of precipitation and groundwater storage increases with temporal scale, with the effect of precipitation decreasing from annual to seasonal and to monthly scales. The behavior of the equitant regions (between water-limited and energy-limited) for precipitation and groundwater storage lies between the two regimes (Figure 4 and Supporting Information, Figure S7). The contribution of potential evaporation does not noticeably change with different climate regions. These results suggest that for the dry and equitant regions, groundwater storage is vital to the resilience of streamflow under changing climate.

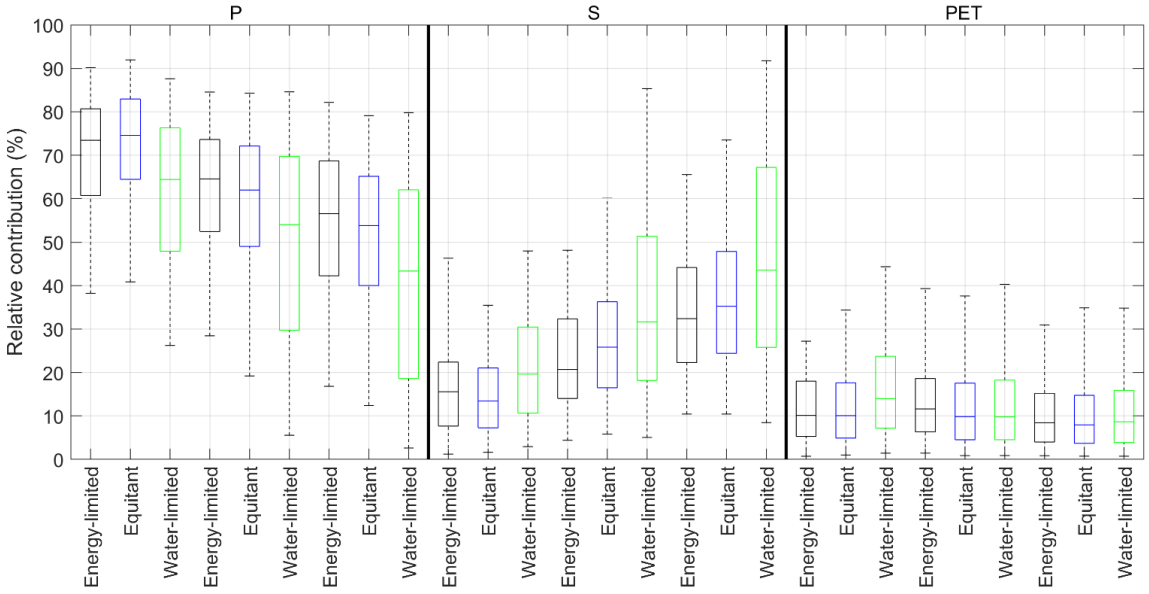

Figure 4. Use of aridity index to stratify the relative contributions of precipitation (P), groundwater storage (S) and potential evaporation (PET) to streamflow variability. Black, blue and green boxes represent annual, seasonal and monthly scales, respectively. Three climatic regions are defined: energy-limited (aridity index, AI < 0.76), equitant ($0.76 \leq AI \leq 1.35$) and water-limited (AI > 1.35). Data are from 1628 catchments using 15 approaches. For each boxplot, the bottom, middle, and top of the box are the 25th, 50th, and 75th percentiles, and the bottom and top whiskers show the 5th and 95th percentiles.

4.3. Spatial Pattern

There is a distinct geographic pattern across the globe where streamflow resilience is enhanced by groundwater storage, which is indicated by the streamflow elasticities and the corresponding contributions of precipitation, groundwater storage and potential evaporation to streamflow variability (Figure 5). At annual scale,

most catchments located in Australia, Europe and the eastern United States are highly sensitive to precipitation, which is the largest contributor to streamflow variability. However, groundwater storage and potential evaporation are dominant in eastern China, the western United States, and western Canada. At seasonal scale, precipitation is still dominant in the eastern United States and some European and Australian catchments, but groundwater storage plays a major role in the western United States and Eastern China. At monthly scale, groundwater storage outweighs precipitation in most catchments, except for those located in parts of the eastern United States where precipitation continues to dominate the streamflow variation. Analysis using different potential evaporation and groundwater storage methods shows very similar spatial patterns (Supporting Information, Figures S8–S21).

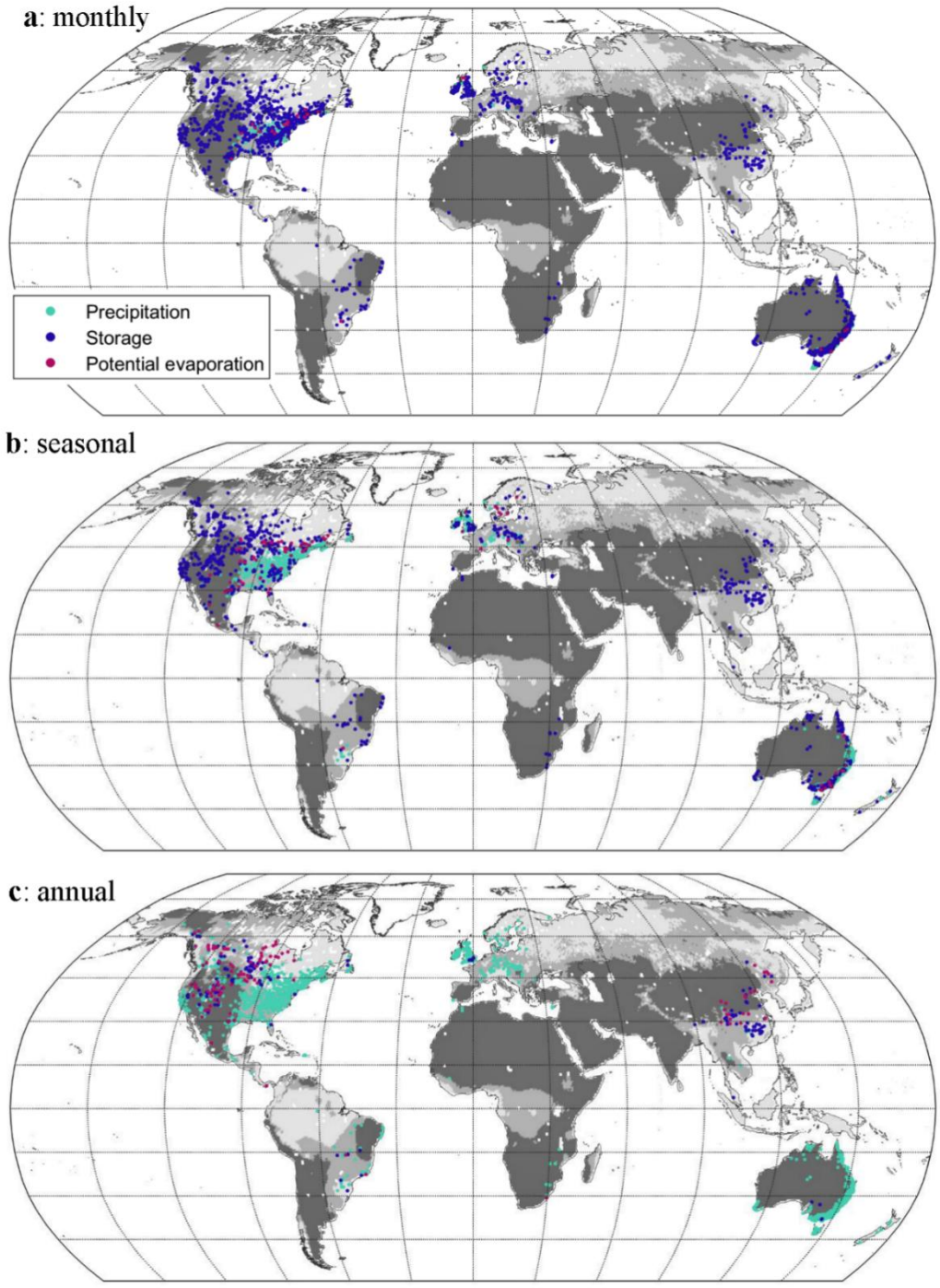

Figure 5. The largest contributing factor to the variability of streamflow. (**a**) monthly scale. (**b**) seasonal scale. (**c**) annual scale. Cyan, blue and red are for precipitation, storage and potential evaporation, respectively. Energy-limited (aridity index, AI < 0.76), equitant (0.76 ≤ AI ≤ 1.35) and water-limited (AI > 1.35) regions are represented by light grey, grey, and dark grey. The result is obtained from one approach that uses Lyne-Hollick storage and Penman potential evaporation.

4.4. Evaluating Global Model Performance

The above sections are obtained from the data-driven framework. Since many global hydrological or earth system models used in climate change projections represent groundwater fluxes using simple groundwater models, it is pertinent to ask whether these models may be used to investigate streamflow elasticity from monthly to annual scales. To address this question, we use the monthly, seasonal and annual groundwater recharge estimated from four global hydrological models [28] together with their forcing data of precipitation and potential evaporation to repeat the analysis of attributing streamflow variations to precipitation, potential evaporation, and groundwater storage (see Methods section). Using groundwater storage from global models produces similar attribution of streamflow variations at annual and seasonal scales as our earlier analysis based entirely on observations, but lower fractions of streamflow variations are now explained at monthly and seasonal scales (Supporting Information, Figures S22 and S23). It is interesting to note that using the global model results strengthens the finding that the contribution of groundwater storage is stronger in water-limited regions than in energy-limited regions (Supporting Information, Figure S28). However, global models cannot identify the increasing precipitation elasticity and the decreasing storage elasticity from monthly to annual scales (Supporting Information, Figures S24–S28). This demonstrates that the current generation of global models cannot be used to reliably simulate monthly streamflow variability and the response of monthly streamflow to environmental changes [53,54].

Our research therefore suggests an urgent need to improve global land surface models used in global climate models for more realistic modeling of monthly groundwater recharge when simulating the hydrological consequence of climate variability [11,55,56]. It will be essential to test these models against monthly streamflow observations at many gauges around the world. Our analysis provides guidance on the regions where this is most important. Improving groundwater modeling will allow land surface models to be more useful for supporting climate adaptation strategies [57,58].

5. Discussion

Precipitation is ultimately the source of catchment streamflow. This is especially true at longer temporal scales from annual to decades as the changes in groundwater storage tend to be small [59]. At subannual temporal scale, the hydrological behavior of catchment is more tangibly regulated by storage [12,21,22,24,51,60], which is the underlying cause of the scale-dependent precipitation elasticity of streamflow. Streamflow resilience with respect to climate variation assessed using annual-scale elasticity could overestimate the impact of precipitation change on monthly or seasonal streamflow. This is because not all precipitation turns into streamflow instantly after a storm event. Quite the contrary, a proportion of the rainfall recharges the aquifer and is subsequently released gradually as baseflow after the event. Even though at a longer period, the storage sourced from precipitation and its contribution to streamflow are amalgamated into the total precipitation contribution, the storage contribution to streamflow could be as important as the direct contribution from precipitation in governing short-term streamflow.

There are other types of surface storage that might affect the observed streamflow variation in some study catchments, including lakes, snow, and ice. We acknowledge that these surface storages might influence the performance of our analysis framework, particularly in catchments where storage by lakes, snow, and ice is more significant than groundwater storage. However, it is expected to have little impact on our conclusion since overall, our framework performs almost equally well at the three temporal scales (Supporting Information, Figure S1).

As groundwater storage plays an essential role in shaping streamflow resilience to climate variability at monthly scale, it is critical to improve monitoring and management of that storage [61,62]. The streamflow resilience can be enhanced by increasing catchment storage during the wet season. This is particularly crucial for catchments with storage deficits and that are subject to seasonal drought threats. For these catchments, options such as artificial flood recharge could be considered to increase storage and enhance resilience. In adaptation to climate change, water planners could increase infiltration in urbanized area with a high degree of impervious surface coverage and compacted soils [63–65] by recharging ponds and planting vegetation that enhances the connectivity between the surface and ground water [24,66,67].

6. Conclusions

There are numerous studies carried out to investigate streamflow variation at annual to decadal timescales. It remains unclear how the streamflow variability at subannual scales is influenced by different drivers. This study estimates streamflow elasticities to three drivers (precipitation, potential evaporation and groundwater storage) and streamflow variability at monthly to annual scales using the elasticity framework. Using data from 1628 unregulated catchments distributed across the globe, we find that the elasticity of streamflow to groundwater

storage at monthly and seasonal scales is far larger than the annual elasticity, especially in water limited regions. The temporal scale effect of groundwater storage causes smaller elasticity of streamflow to precipitation at subannual scales than at annual scale. Therefore, groundwater storage must be combined with precipitation and potential evaporation to provide a comprehensive perspective of the streamflow response to climate variability and change. Our research therefore suggests an urgent need to improve global land surface models used in global climate models for more realistic modeling of monthly groundwater recharge when simulating the hydrological consequence of climate variability.

Supplementary Materials

The additional data and information can be downloaded at: https://media.sciltp.com/articles/others/25091115 16060582/HWR-2508000002-SI-FC.pdf. Figure S1: Summary of the performance of the multi-temporal framework for attributing streamflow variation in all 1628 catchments, for each of the 15 approaches used. Figure S2: Comparisons of observed annual streamflow variability (ΔQ, in mm/year) with that estimated (mm/year) from all three drivers (precipitation, groundwater storage and potential evaporation) and at three temporal scales (annual, seasonal and monthly). The ΔQ_i is taken as the sum of $\Delta Q_{i,j}$ where i is for the i^{th} year and j is for the j^{th} month (or season) (see Equation (2)). Data are obtained from all 1628 catchments and 15 approaches. Figure S3: Comparisons of streamflow elasticity between monthly and annual scales and comparisons of the relative contributions of the three variables obtained from 15 methods. (a). Precipitation elasticity of streamflow (ϵ_P) between monthly and annual scales. (b). Groundwater storage elasticity of streamflow (ϵ_S) between monthly and annual scales. (c). Potential evaporation elasticity of streamflow (ϵ_{PET}) between monthly and annual scales. (d). Relative contribution of precipitation between monthly and annual scales. €. Relative contribution of groundwater storage between monthly and annual scales. (f). Relative contribution of potential evaporation between monthly and annual scales. Each closed contour indicates the probability of occurrence of the variables being compared in (a–f). Figure S4: Same as Figure S3, but for comparisons between seasonal and annual scales. Figure S5: Same as Figure S3, but for the comparisons between monthly and seasonal scales. Figure S6: Comparisons between relative contribution of catchment storage (RC_S) and relative contribution of precipitation (RC_p) at three temporal scales: monthly, seasonal and annual. Figure S7: Relative contribution (%) of precipitation (P), groundwater storage (S) and potential evaporation (PET) to streamflow variability at monthly (a,d,g), seasonal (b,e,h) and annual (c,f,i) scales for different climate regimes (top three panels (a–c) for energy-limited, middle three panels (d–f) for equitant, bottom three panels (g–i) for water-limited) and for all combinations of catchments and approaches (1268 catchments × 15 approaches). The space enclosed by the contours corresponds to 10%, 30%, 50%, 70% and 90% probability. The number of points (count) is indicated using a filled color in each hexagon bin. The sum of the three contributions is 100%. Figure S8: The largest contribution factor to the streamflow variability. a. monthly scale. b. seasonal scale. b. annual scale. Cyan, blue and red are for precipitation, storage and potential evaporation, respectively. Energy-limited (aridity index, AI < 0.76), equitant (0.76 ≤ AI ≤1.35) and water-limited (AI >1.35) regions are represented by light grey, grey, and dark grey. The results are obtained from one approach that uses Boughton-Chapman storage and Penman potential evaporation. Figure S9: Same as Figure S8, but obtained from the method using Chapman-Maxwell storage and Penman potential evaporation. Figure S10: Same as Figure S8, but obtained from the method using Eckhard storage and Penman potential evaporation. Figure S11: Same as Figure S8, but obtained from the method using Standard storage and Penman potential evaporation. Figure S12: Same as Figure S8, but obtained from the method using Boughton-Chapman storage and Priestley-Taylor potential evaporation. Figure S13: Same as Figure S8, but obtained from the method using Chapman-Maxwell storage and Priestley-Taylor potential evaporation. Figure S14: Same as Figure S8, but obtained from the method using Eckhard storage and Priestley-Taylor potential evaporation. Figure S15: Same as Figure S8, but obtained from the method using Lyne-Hollick storage and Priestley-Taylor potential evaporation. Figure S16: Same as Figure S8, but obtained from the method using Standard storage and Priestley-Taylor potential evaporation. Figure S17: Same as Figure S8, but obtained from the method using Boughton-Chapman storage and Morton potential evaporation. Figure S18: Same as Figure S8, but obtained from the method using Chapman-Maxwell storage and Morton potential evaporation. Figure S19: Same as Figure S8, but obtained from the method using Eckhard storage and Morton potential evaporation. Figure S20: Same as Figure S8, but obtained from the method using Lyne-Hollick storage and Morton potential evaporation. Figure S21: Same as Figure S8, but obtained from the method using Standard storage and Morton potential evaporation. Figure S22: Same as Figure S1, but obtained from groundwater recharge simulated from four global hydrological models together with their forcing data of precipitation and potential evaporation in 1351 catchments. Note that there are 277 of 1628 catchments without the global hydrological model outputs and therefore they were eliminated for the analysis. Figure S23: Same as Figure S2, but ΔQ obtained from groundwater recharge simulated from four global hydrological models together with their forcing data of precipitation and potential evaporation in 1351 catchments. There are total of 4 combinations obtained from the four global hydrological models. Figure S24: Same as Figure S2, but the elasticity obtained from groundwater recharge simulated from four global hydrological models together with their forcing data of precipitation and potential evaporation in 1351 catchments. There are total of 4 combinations obtained from the four global hydrological models. Figure S25: Same as Figure S24, but for the comparisons between seasonal and

annual scales. Figure S26: Same as Figure S24, but for the comparisons between monthly and seasonal scales. Figure S27: Same as Figure S6, but the relative contributions obtained from groundwater recharge simulated from four global hydrological models together with their forcing data of precipitation and potential evaporation in 1351 catchments. There are total of 4 combinations obtained from the four global hydrological models. Figure S28: Same as Figure S7 for monthly (a,d,g), seasonal (b,e,h) and annual (c,f,i) scales and for different climate regimes (top three panels (a–c) for energy-limited, middle three panels (d–f) for equitant, bottom three panels (g–i) for water-limited), but the relative contributions obtained from precipitation, potential evaporation, and groundwater recharge simulated from four global hydrological models in 1628 catchments. There are total of 4 combinations obtained from the four global hydrological models.

Author Contributions

Y.Z.: conceptualization, methodology, data curation, writing—original draft preparation; H.Z.: methodology, data curation, writing—original draft preparation; C.L.: conceptualization, writing—reviewing and editing, L.L.: conceptualization, writing—reviewing and editing; CMZ: conceptualization, writing—reviewing and editing; D.K.: visualization, data curation, investigation; G.B.: conceptualization, writing—reviewing and editing. All authors have read and agreed to the published version of the manuscript.

Funding

Y.Z. is supported by the "Quantifying Groundwater Changes and Development of Better Agricultural Water Saving Techniques in the Western Ordos" Program funded by the Bureau of Science and Technology of the Erdos (Grant No. ZD20232302) and by the Talent Program of the Ministry of Science and Technology of China. L.L. is supported by the Office of Science, U.S. Department of Energy, Biological and Environmental Research as part of the Regional and Global Model Analysis program area. PNNL is operated for the Department of Energy by Battelle Memorial Institute under contract DE-AC05-76RL01830. C.Z. is supported by the funding agencies of Zhejiang Province and Ningbo Municipality through the program "Novel technologies for joint pollution reduction and carbon sequestration."

Institutional Review Board Statement

Not applicable.

Informed Consent Statement

Not applicable.

Data Availability Statement

The streamflow data used in this study were obtained from Global Runoff Data Centre (GRDC, https://www.bafg.de/GRDC/EN/Home/homepage_node.html), Geospatial Attributes of Gages for Evaluating Streamflow (GAGES)-II database (https://water.usgs.gov/GIS/metadata/usgswrd/XML/gagesII_Sept2011.xml), and the Australian Bureau of Meteorology (http://www.bom.gov.au/waterdata/). We also thank the Princeton Global forcing group for providing climate datasets (https://hydrology.princeton.edu/data.pgf.php).

The catchment attribute and estimated elasticity datasets are available from the following link:

https://media.sciltp.com/files/content/Catchment_Attributes_1628.xlsx, which includes catchment ID, geographic coordinates of river gage, catchment area, elevation, period of data used in our analysis (start date and end date), average streamflow rates (m^3/s), recession constant, aridity index, climate conditions (humid, equitant, dry) , and elasticity values at three temporal scales (monthly, seasonal, annual).

Acknowledgments

We thank the editors and anonymous reviewers for their constructive feedback, and we are grateful to the state water agencies and research organizations that provided the streamflow data used in this study.

Conflicts of Interest

The authors declare that they have no competing interests.

References

1. Berghuijs, W.R.; Woods, R.A.; Hrachowitz, M.; et al. A precipitation shift from snow towards rain leads to a decrease in streamflow. *Nat. Clim. Chang.* **2014**, *4*, 583–586.
2. Blöschl, G.; Hall, J.; Parajka, J.; et al. Changing climate shifts timing of European floods. *Science* **2017**, *357*, 588–590.

3. Haddeland, I.; et al. Global water resources affected by human interventions and climate change. *Proc. Natl. Acad. Sci. USA* **2014**, *111*, 3251–3256.
4. Mekonnen, M.M.; Hoekstra, A.Y. Four billion people facing severe water scarcity. *Sci. Adv.* **2016**, *2*, e1500323.
5. Milly, P.C.D.; Betancourt, J.; Falkenmark, M.; et al. Climate change - Stationarity is dead: Whither water management? *Science* **2008**, *319*, 573–574.
6. Munoz, S.E.; Giosan, L.; Therrell, M.D.; et al. Climatic control of Mississippi River flood hazard amplified by river engineering. *Nature* **2018**, *556*, 95–98.
7. Zhang, Y.; Li, C.; Chiew, F.H.S.; et al. Southern Hemisphere dominates recent decline in global water availability. *Science* **2023**, *382*, 579–584.
8. Griggs, D.; Stafford-Smith, M.; Gaffney, O.; et al. Sustainable development goals for people and planet. *Nature* **2013**, *495*, 305.
9. Arheimer, B.; Donnelly, C.; Lindstrom, G.; et al. Regulation of snow-fed rivers affects flow regimes more than climate change. *Nat. Commun.* **2017**, *8*, 62.
10. Dai, A.G. Increasing drought under global warming in observations and models. *Nat. Clim. Chang.* **2013**, *3*, 52–58.
11. Milly, P.C.D.; Dunne, K.A.; Vecchia, A.V.; et al. Global pattern of trends in streamflow and water availability in a changing climate. *Nature* **2005**, *438*, 347–350.
12. Stocker, B.D.D.; Tumber-Davila, S.J.; Konings, A.G.G.; et al. Global patterns of water storage in the rooting zones of vegetation. *Nat. Geosci.* **2023**, *16*, 250–256.
13. Zhou, G.; Wei, X.; Chen, X.; et al. Global pattern for the effect of climate and land cover on water yield. *Nat. Commun.* **2015**, *6*, 5918. https://doi.org/10.1038/ncomms6918.
14. Ahlstrom, A.; Canadell, J.G.; Schurgers, G.; et al. Hydrologic resilience and Amazon productivity. *Nat. Commun.* **2017**, *8*, 387.
15. Botter, G.; Basso, S.; Rodriguez-Iturbe, I.; et al. Resilience of river flow regimes. *Proc. Natl. Acad. Sci. USA* **2013**, *110*, 12925–12930.
16. Fu, G.; Charles, S.P.; Chiew, F.H.S.; et al. A two-parameter climate elasticity of streamflow index to assess climate change effects on annual streamflow. *Water Resour. Res.* **2007**, *43*, W11419. https://doi.org/10.1029/2007WR005890.
17. Sankarasubramanian, A.; Vogel, R.M.; Limbrunner, J.F.; et al. Climate elasticity of streamflow in the United States. *Water Resour. Res.* **2001**, *37*, 1771–1781.
18. Zheng, H.; Zhang, L.; Zhu, R.; et al. Responses of streamflow to climate and land surface change in the headwaters of the Yellow River Basin. *Water Resour. Res.* **2009**, *45*, W00A19. https://doi.org/10.1029/2007WR006665.
19. Ukkola, A.M.; Prentice, I.C.; Keenan, T.F.; et al. Reduced streamflow in water-stressed climates consistent with CO_2 effects on vegetation. *Nat. Clim. Chang.* **2016**, *6*, 75–78.
20. Andermann, C.; Longuevergne, L.; Bonnet, S.; et al. Impact of transient groundwater storage on the discharge of Himalayan rivers. *Nat. Geosci.* **2012**, *5*, 127–132.
21. Berghuijs, W.R.; Hartmann, A.; Woods, R.A.; et al. Streamflow sensitivity to water storage changes across Europe. *Geophys. Res. Lett.* **2016**, *43*, 1980–1987.
22. Condon, L.E.; Maxwell, R.M. Simulating the sensitivity of evapotranspiration and streamflow to large-scale groundwater depletion. *Sci. Adv.* **2019**, *5*, eaav4574.
23. de Graaf, I.E.M.; Gleeson, T.; van Beek, L.P.H.; et al. Environmental flow limits to global groundwater pumping. *Nature* **2019**, *574*, 90–94.
24. Maxwell, R.M.; Condon, L.E. Connections between groundwater flow and transpiration partitioning. *Science* **2016**, *353*, 377–380.
25. Scanlon, B.R.; Levitt, D.G.; Reedy, R.C.; et al. Ecological controls on water-cycle response to climate variability in deserts. *Proc. Natl. Acad. Sci. USA* **2005**, *102*, 6033–6038.
26. Scanlon, B.R.; Zhang, Z.; Save, H.; et al. Global models underestimate large decadal declining and rising water storage trends relative to GRACE satellite data. *Proc. Natl. Acad. Sci. USA* **2018**, *115*, E1080–E1089.
27. Sheffield, J.; Goteti, G.; Wood, E.F.; et al. Development of a 50-year high-resolution global dataset of meteorological forcings for land surface modeling. *J. Clim.* **2006**, *19*, 3088–3111.
28. Schellekens, J.; Dutra, E.; Martínez-de La Torre, A.; et al. A global water resources ensemble of hydrological models: the eartH_2Observe Tier-1 dataset. Earth Syst. *Sci. Data* **2017**, *9*, 389–413.
29. Priestley, C.; Taylor, R. On the assessment of surface heat flux and evaporation using large-scale parameters. *Mon. Weather Rev.* **1972**, *100*, 81–92.
30. Penman, H.L. Evaporation: an introductory survey. *Neth. J. Agric. Sci.* **1956**, *4*, 9–29.
31. Morton, F.I. Operational estimates of lake evaporation. *J. Hydrol.* **1983**, *66*, 77–100.
32. Beck, H.E.; van Dijk, A.I.J.M.; de Roo, A.; et al. Global-scale regionalization of hydrologic model parameters. *Water Resour. Res.* **2016**, *52*, 3599–3622.

33. Zhang, Y.; Peña-Arancibia, J.L.; McVicar, T.R.; et al. Multi-decadal trends in global terrestrial evapotranspiration and its components. *Sci. Rep.* **2016**, *6*, 19124. https://doi.org/10.1038/srep19124.
34. Falcone, J.A.; Carlisle, D.M.; Wolock, D.M.; et al. GAGES: A stream gage database for evaluating natural and altered flow conditions in the conterminous United States. *Ecology* **2010**, *91*, 621–621.
35. Lehner, B.; et al. High-resolution mapping of the world's reservoirs and dams for sustainable river-flow management. *Front. Ecol. Environ.* **2011**, *9*, 494–502.
36. Beck, H.E.; Dijk, A.I.J.M.; Miralles, D.G.; et al. Global patterns in base flow index and recession based on streamflow observations from 3394 catchments. *Water Resour. Res.* **2013**, *49*, 7843–7863.
37. Chiew, F.H.S.; Peel, M.C.; Western, A.W.; et al. *Mathematical Models of Small Watershed Hydrology and Applications*; Singh, V.P., Frevert, D.K., Eds.; Water Resources Publication: St. John's, NL, Canada, 2022; pp. 335–367.
38. Chapman, T. A comparison of algorithms for stream flow recession and baseflow separation. *Hydrol. Process.* **1999**, *13*, 701–714.
39. Van Dijk, A.I.J.M.; Peña-Arancibia, J.L.; Wood, E.F.; et al. Global analysis of seasonal streamflow predictability using an ensemble prediction system and observations from 6192 small catchments worldwide. *Water Resour. Res.* **2013**, *49*, 2729–2746.
40. Fenicia, F.; Savenije, H.H.G.; Matgen, P.; et al. Is the groundwater reservoir linear? Learning from data in hydrological modelling. *Hydrol. Earth Syst. Sci.* **2006**, *10*, 139–150.
41. Gustard, A.; Roald, L.A.; Demuth, S.; et al. *Flow Regimes from Experimental and Network Data (FREND*); Volume I: Hydrological Studies; IAHS Press: Wallingford, UK, 1989.
42. Lyne, V.; Hollick, M. Stochastic Time-Variable Rainfall-Runoff Modeling. *Inst. Eng. Aust. Natl. Conf.* **1979**, *79*, 89–93.
43. Boughton, W.C. *A Hydrograph-Based Model for Estimating the Water Yield of Ungauged Catchments, Hydrology and Water Resources Symposium*; IEAust: Newcastle, UK, 1993.
44. Eckhardt, K. How to construct recursive digital filters for baseflow separation. *Hydrol. Process.* **2005**, *19*, 507–515.
45. Nathan, R.J.; McMahon, T.A. Evaluation of automated techniques for base flow and recession analyses. *Water Resour. Res.* **1990**, *26*, 1465–1473.
46. Lindström, G.; Johansson, B.; Persson, M.; et al. Development and test of the distributed HBV-96 hydrological model. *J. Hydrol.* **1997**, *201*, 272–288.
47. Van Der Knijff, J.M.; Younis, J.; De Roo, A.P.J.; et al. LISFLOOD: A GIS-based distributed model for river basin scale water balance and flood simulation. *Int. J. Geogr. Inf. Sci.* **2010**, *24*, 189–212.
48. Sutanudjaja, E.H.; Van Beek, R.; Wanders, N.; et al. PCR-GLOBWB 2: A 5 arcmin global hydrological and water resources model. *Geosci. Model Dev.* **2018**, *11*, 2429–2453.
49. Decharme, B.; Alkama, R.; Douville, H.; et al. Global Evaluation of the ISBA-TRIP Continental Hydrological System. Part II: Uncertainties in River Routing Simulation Related to Flow Velocity and Groundwater Storage. *J. Hydrometeorol.* **2010**, *11*, 601–617.
50. Hamilton, N.E.; Ferry, M. ggtern: Ternary Diagrams Using ggplot2. *J. Stat. Sofrware* **2018**, *87*, 1–17. https://doi.org/10.18637/jss.v087.c03.
51. Buttle, J.M. Mediating stream baseflow response to climate change: The role of basin storage. *Hydrol. Process.* **2018**, *32*, 363–378.
52. Price, K. Effects of watershed topography, soils, land use, and climate on baseflow hydrology in humid regions: A review. *Prog. Phys. Geogr.* **2011**, *35*, 465–492.
53. Gudmundsson, L.; et al. Comparing Large-Scale Hydrological Model Simulations to Observed Runoff Percentiles in Europe. *J. Hydrometeorol.* **2011**, *13*, 604–620.
54. Humphrey, V.; Zscheischler, J.; Ciais, P.; et al. Sensitivity of atmospheric CO2 growth rate to observed changes in terrestrial water storage. *Nature* **2018**, *560*, 628–631.
55. Betts, R.A.; Boucher, O.; Collins, M.; et al. Projected increase in continental runoff due to plant responses to increasing carbon dioxide. *Nature* **2007**, *448*, 1037–1041.
56. Taylor, R.G.; Scanlon, B.; Döll, P.; et al. Ground water and climate change. *Nat. Clim. Chang.* **2013**, *3*, 322–329.
57. Reager, J.T.; Gardner, A.S.; Famiglietti, J.S.; et al. A decade of sea level rise slowed by climate-driven hydrology. *Science* **2016**, *351*, 699–703.
58. Rodell, M.; Famiglietti, J.S.; Wiese, D.N.; et al. Emerging trends in global freshwater availability. *Nature* **2018**, *557*, 650–658.
59. Zhang, L.; Dawes, W.R.; Walker, G.R.; et al. Response of mean annual evapotranspiration to vegetation changes at catchment scale. *Water Resour. Res.* **2001**, *37*, 701–708.
60. Huggins, X.; Gleeson, T.; Serrano, D.; et al. Overlooked risks and opportunities in groundwatersheds of the world's protected areas. *Nat. Sustain.* **2023**, *6*, 855–864.

61. Mohan, C.; Gleeson, T.; Forstner, T.; et al. Quantifying Groundwater's Contribution to Regional Environmental-Flows in Diverse Hydrologic Landscapes. *Water Resour. Res.* **2023**, *59*, e2022WR033153.
62. Xingxing Kuang et al. The changing nature of groundwater in the global water cycle. ***Science*** **2024**, *383*, eadf0630.
63. Bai, X.M.; Shi, P.J.; Liu, Y.S.; et al. Realizing China's urban dream. *Nature* **2014**, *509*, 158–160.
64. Larsen, T.A.; Hoffmann, S.; Luthi, C.; et al. Emerging solutions to the water challenges of an urbanizing world. *Science* **2016**, *352*, 928–933.
65. Song, X.P.; Hansen, M.C.; Stehman, S.V.; et al. Global land change from 1982 to 2016. *Nature* **2018**, *560*, 639–643.
66. Good, S.P.; Noone, D.; Bowen, G.; et al. Hydrologic connectivity constrains partitioning of global terrestrial water fluxes. *Science* **2015**, *349*, 175–177.
67. Remesan, R.; Bellerby, T.; Holman, I.; et al. WRF model sensitivity to choice of parameterization: a study of the 'York Flood 1999'. *Theor. Appl. Climatol.* **2015**, *122*, 229–247.